A new observational evidence of generation and propagation of barotropic Rossby waves induced by tropical instability waves in the Northeastern Pacific

Kang-Nyeong Lee[1], Chanhyung Jeon[2], YoungHo Seung[1], Hong-Ryeol Shin[3], Seung-Kyu Son[4], and Jae-Hun Park[1*]

[1]Department of Ocean Sciences, Inha University, Incheon 22212, South Korea.

[2] Department of Oceanography, Pusan National University, Busan 46241, South Korea.

[3]Department of Atmospheric Sciences, Kongju National University, Kongju 32588, South Korea.

[4]Deep-sea and Seabed Mineral Resources Research Center, Korea Institute of Ocean Science & Technology, Busan 49111, South Korea.

Corresponding author: Jae-Hun Park (jaehunpark@inha.ac.kr)

Key Points:

- In-situ near-bottom current velocity records are coherent with satellite-measured sea surface height related to tropical instability waves.
- The near-bottom current variations are likely caused by northward propagating tropical instability wave-induced barotropic Rossby waves.
- Tropical instability wave-induced barotropic Rossby waves vary inter-annually with maxima during the La Niña periods.

Abstract

Tropical instability waves (TIWs) in the equatorial eastern Pacific (EEP) exhibit 25–40-day westward-propagating fluctuations with seasonal and inter-annual variations, which are stronger during July−December and La Niña periods. They likely transfer their energy northward by forming barotropic Rossby waves (BTRWs). Long-term near-bottom current measurements at 10.5°N and 131.3°W during 2004–2013 revealed a spectral peak at 25–40 days, where significant coherences were found with satellite-measured sea surface height in a wide region of EEP with maxima approximately 5°N. Simulated deep currents from a data-assimilated ocean model concur with the observed near-bottom currents, and both currents vary seasonally and interannually, consistent with the typical characteristics of TIW. Further analyses using 25–40-day bandpass-filtered barotropic velocity data from the model revealed that they reasonably satisfied the theoretical dispersion relation of TIW-induced BTRW ($BTRW_{TIW}$). We reconfirmed $BTRW_{TIW}$ propagating northward above 10°N in the northeastern Pacific by in-situ observations.

Plain Language Summary

Tropical instability waves (TIWs), which are located at the boundary between the warm pool and the cold tongue in the eastern Pacific, propagate westward with 25–40-day periods and vary seasonally and interannually, which are stronger during July–December and La Niña periods. Near-bottom velocity measured over a 10-year period at 10.5°N, 131.3°W just above the northern boundary of the waves fluctuates with 25–40-day periods, coinciding with that of sea surface height (SSH) in the equatorial eastern Pacific, especially around 5°N. We find that the wavelike pattern has wave crests oriented southeast-northwest from the model, and that this pattern appears across the study area and has characteristics consistent with TIWs including seasonal and interannual variations with the typical wavenumber and frequency. This pattern was verified to be a barotropic Rossby wave (BTRW) through a model result analysis. Thus, TIWs induce BTRWs that transfer their energy to the abyssal ocean above 10°N in the northeastern Pacific. This study provides a new observational evidence that near-bottom currents vary with BTRWs induced by TIW.

1 Introduction

Tropical instability waves (TIWs), which propagate westward and have a cusp-like shape with repetitive high amplitudes near 5°N around the boundary of the cold tongue in the equatorial eastern Pacific Ocean, can be observed using satellite-measured sea surface temperature (Legeckis, 1977; Legeckis et al., 1983) and sea surface height (SSH) (Lyman et al., 2005; Farrar, 2011; Holmes and Thomas, 2016; Tchilibou et al., 2018). It is known that TIWs result from instability by interactions between equatorial current system such as the Equatorial Undercurrent, the South Equatorial Current, the North Equatorial Current, and the North Equatorial Countercurrent (Philander, 1976; Lyman et al., 2005). Previous studies described broad ranges of wavenumber and frequency of TIWs depending on measurements utilized for them. Lee et al. (2017) summarized the previous estimates of the wavenumbers and frequencies of TIWs over the spectrum and reported that the TIWs observed by SSH measurements show peak near periods of 33 days and wavelengths of 12°–16° in the wavenumber-frequency spectrum.

The waves are representative phenomena with intraseasonal periods in the tropical eastern Pacific Ocean, although these properties are not always remarkable (Chelton et al., 2000; An, 2008; Shinoda et al., 2009). TIWs exhibit seasonal variations in the occurrence of intense growth from July to December, with more energetic activities during La Niña periods, linked to the strengthening of upwelling in response to strong trade winds in the equatorial eastern Pacific (Contreras, 2002; Warner & Moum, 2019).

Previous studies have focused mainly on the effects of TIWs near the equatorial ocean because it is known that the waves play an important role in regional ecosystems and the balance of heat associated with advection in the equatorial surface ocean (Willett et al., 2006; Moum et al., 2009). However, Farrar (2011) identified that TIWs can affect their energy up to approximately 20°N. The longitude-time band-pass filtered SSH shows a structure of TIW at 0°−10°N and a propagation of barotropic Rossby waves (BTRWs) induced by TIW north of 10°N. Furthermore, using both results from barotropic ocean model and newly gridded satellite-measured SSH with a mapping algorithm without latitudinal variation in its filtering properties, Farrar et al. (2021) showed that the propagation of the BTRWs continues until 35°N. However, these studies lacked in-situ observations.

Here, we used 10-year-long in-situ near-bottom current measurements that were recorded at a site located north away from the active region of TIW. The in-situ near-bottom current measurements clearly show that the energy of the TIW-induced BTRWs propagate northward. The processes of energy propagation in the form of BTRWs were also analyzed through the satellite-measured SSH as well as the results of data-assimilated numerical simulation (GLORYS12V1). In addition, the long-term in-situ measurements, satellite measurements, and results of GLORYS12V1 between 2004 and 2013 enable the verification of interannual variations according to the El Niño-Southern Oscillation (ENSO).

2 Data and Methods

2.1 In-situ and satellite measurements and GLORYS12V1 model results

Long-term, half-hour interval near-bottom current data (U_{obs}, V_{obs}) were recorded at a depth of ~5000 m in the northeastern Pacific (10.5°N, 131.3°W; black star in Figure 1a) from August 21, 2004 to July 27, 2013. The observations were conducted as part of the Korea Deep Ocean Study (KODOS). To compare in-situ data with other data explained below, the former were averaged over a day.

Farrar et al. (2021) noted that the SSH data product by Copernicus Climate Change Service causes barotropic signals with 30-day periods to disappear at higher than 20°N due to a mapping algorithm. They produced a special-purpose gridded SSH product which has latitudinally uniform filtering properties. In this paper, we used the newly gridded SSH data product (hereafter referred to as Farrar SSH) with a space-time grid of 0.5° × 0.5° × 3 days to conduct the spectral analysis and squared coherency analysis with our in-situ data subsampled at a 3-day interval. The domain used was 0°–20°N and 140°–80°W during the same period of near-bottom current measurements.

We also used the results of a data-assimilated global ocean reanalysis numerical simulation (GLORYS12V1) to investigate the characteristics of TIW-induced BTRWs. The GLORYS12V1 product is provided by the Copernicus Marine Environment Monitoring Service (CMEMS), and its component is the Nucleus for a European Model of the Ocean (NEMO) platform. The daily mean GLORYS12V1 outputs have a spatial resolution of 1/12° × 1/12°. The selected domain for the analyses is the same as that of Farrar SSH, but the data cover the period from January 1, 2004 to December 31, 2013. The velocity results at 4833-m depth filtered by using a band-pass filter with cutoff periods of 25–40 days are consistent with filtered in-situ near-bottom current measurements, showing high correlation of ~0.8.

2.2 Pre-processing of squared coherency

The squared coherency (hereafter referred to as coherence) between Farrar SSH and the time series of in-situ near-bottom current measurements was performed as follows. Spectral analysis was applied to 1088 -long time series with 3-day interval from August 21, 2004, to July 27, 2013. A hamming window of length 192 days was used on the segment, and a 50% overlap was used to increase the number of segments. The 95% significance level, determined by the number of segments and the window, is 0.137 (Thomson & Emery, 2014).

2.3 Complex empirical orthogonal function analysis

The Complex empirical orthogonal function (CEOF) analysis (Hernández-Guerra & Nykjaer, 1997) using the barotropic velocity results, calculated from the depth average of the numerical simulation, requires a preprocessing procedure. The results of the numerical simulation were filtered using a longitude-latitude-time band-pass filter (zonal wavelengths of 9°−20° in longitude, meridional wavelengths of 9°–20° in latitude, and periods of 25–40 days). The longitudinal band-pass filter has a variable cut-off length depending on the latitudes considered; however, the latitudinal band-pass filter has a constant cut-off length for all longitudes. These filtering steps were performed sequentially, first for longitude, next for latitude, and lastly for time. The three dimensions (longitude-latitude-time) filtered data were converted to two dimensions (spatio-temporal section) and the two components were concatenated along the row to consider a spatial relationship between them. The results of CEOF analyses are shown separately for zonal (U_{bt}) and meridional (V_{bt}) components.

3 Results

To compare the Farrar SSH and in-situ near-bottom current velocity (U_{obs},V_{obs}) with each other, two time series of SSH located at different latitudes, indicated by black and red stars in Figure 1a, were used. One is located at the mooring observation site (SSH_{high}), and the other is located at 5°N, 131.3°W (SSH_{low}). Figure 1b shows the time series of Farrar SSH_{low}, SSH_{high}, and in-situ near-bottom current velocity (U_{obs}, V_{obs}) that were filtered by using a band-pass filter with cutoff periods of 25−40 days. Gray lines superimposed on the filtered data show the original time series. The time series corresponding to a red star are surrounded by a box with red dashed lines, and those to a black star are surrounded by a box with black dashed lines. The maximum speed of the original (filtered) U_{obs} and V_{obs} are 13.5 (2.8) cm/s and 16.7 (3.2) cm/s. The filtered time series of U_{obs} and V_{obs} exhibit similar variations to SSH_{low} in approximately a month period, which is consistent with the temporal variation of TIWs reported by Lyman et al., (2007). They are strengthened during the late summer and early winter months, with inter-annual variations. In contrast, the SSH_{high} shows no resemblance to others and has substantially smaller values than the original time series. The results of the spectral analysis also show the same tendency. The spectral peak around the periods of 32 days clearly shows that the filtered time series has the similar periodicity to the TIW (top panels in Figure 1c). In contrast, the power spectral density (PSD) of the SSH_{high} does not show any significant peaks around that period (gray line in Figure 1c).

Coherences between the SSH_{low} and the U_{obs} exhibit a maximum value (> 0.75) at the periods of 32 days and the V_{obs} show higher values (~0.4) than the significance level around the periods of 32 days (middle panel in Figure 1c). In the 32-day periods, the SSH_{low} leads the U_{obs} by 119°, and the V_{obs} leads the SSH_{low} by -7°. Conversely, coherences between the SSH_{high} and either the U_{obs} or the V_{obs} appear to be much smaller than the significance level (0.137) in the 32-day periods. This disparate results seen at two latitudes will be discussed in Figure 3, by using Farrar SSH data and numerical simulation results.

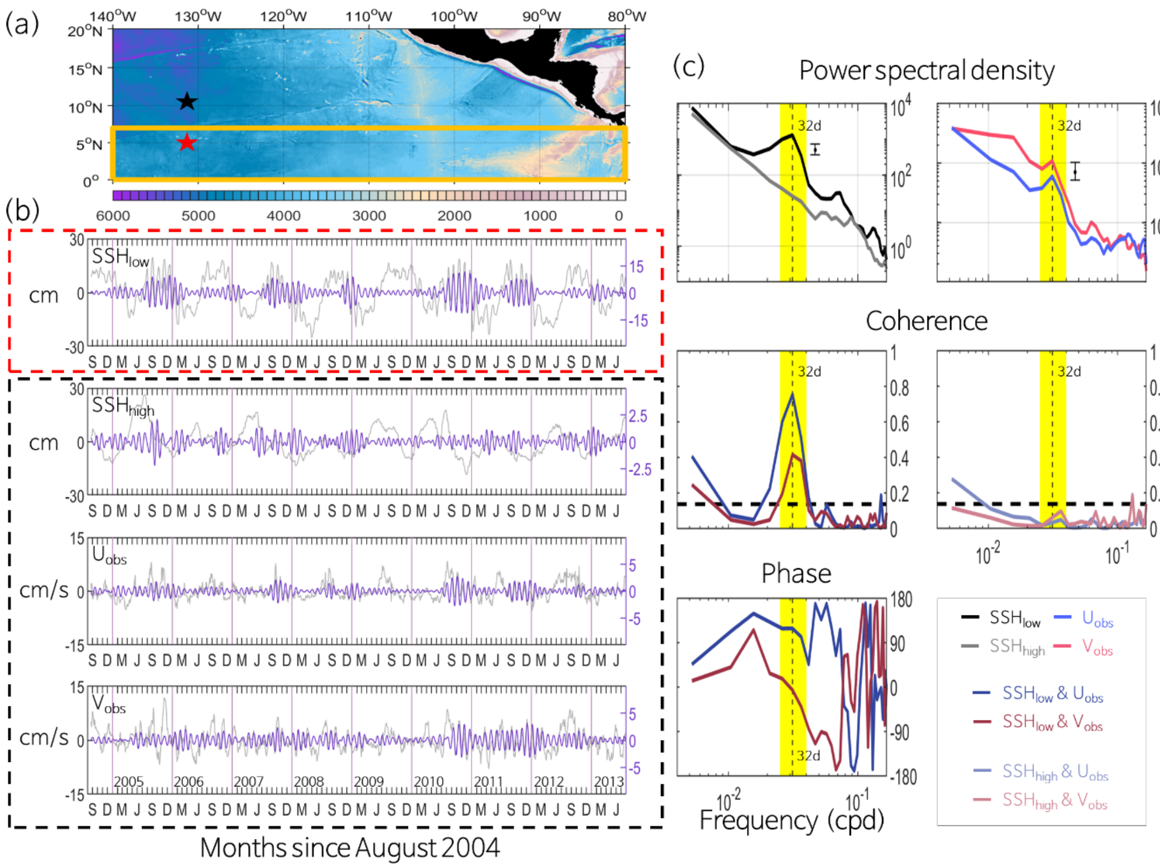

Figure 1. (a) Bathymetry of the numerical model (GLORYS12V1) domain, with black and red stars indicating, respectively, the location of the mooring observation site (10.5°N, 131.3°W) and SSH_{low} (5°N, 131.3°W). (b) Bandpass filtered time series (purple lines) of SSH_{low}, SSH_{high}, U_{obs}, and V_{obs}, having periods of 25–40 days superimposed on their original time series (light gray lines). Note that SSH data are from Farrar et al. (2021) and the color of time series matches with that of the axis of ordinates. (c) Power spectral density of SSH_{low} (black line), SSH_{high} (gray line), U_{obs} (blue line), and V_{obs} (pink line). Vertical bars indicate the 95% confidence interval. Coherences and phases between SSH_{low} and U_{obs} (SSH_{low} and V_{obs}), and SSH_{high} and U_{obs} (SSH_{high} and V_{obs}) are represented by a dark blue line (dark pink line), and a light blue line (light pink line), respectively. The phases between the SSH_{high} and the in-situ near-bottom current data are not shown here because of the low coherences between them. Horizontal dashed lines denote the 95% significance level (0.137). Vertical dashed lines indicate 32-day periods and the yellow shaded areas indicate a TIW frequency band (periods of 25–40 days).

The zonal wavenumber-frequency power spectral density (two-dimensional PSD) averaged over 0°–7°N for Farrar SSH resembles the spectrum shown in Farrar (2011), which is thought to be a common feature associated with the TIW (Figure 2a). The domain used was 0°–7°N, 140°–80°W (yellow box in Figure 1a) and the observation period is from January 1, 2004 to December 31, 2013. Two-dimensional PSDs from longitude-time sections of the data at different latitudes are averaged, resulting in a function of negative zonal wavenumber and frequency (Figure 2). The resulting two-dimensional PSD may allow us to identify the spatio-temporal character of the observed features in the area of active TIWs (the regions surrounded by a yellow box in Figure 1a). Two-dimensional PSDs of the numerical simulation results show high values in the frequency band of periods 25–40 days and in the wavenumber band of wavelength 9°–20° with concentrated values near the 32-day periods (the domains surrounded by the boxes with white lines in Figures 2b–d). It is suggested that TIWs can affect the currents in the deep layer because the distributions of energy of velocity components at 3992-m depth from GLORYS12V1 shows similar characters to those of TIWs.

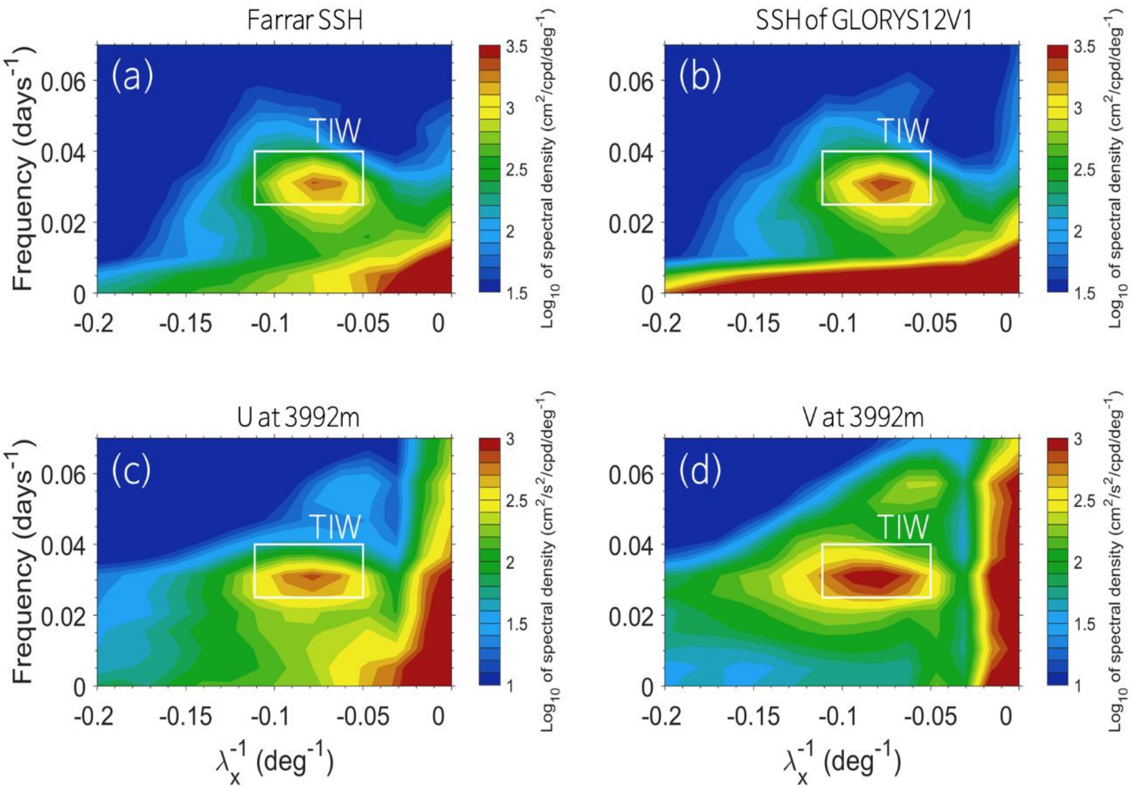

Figure 2. Zonal wavenumber-frequency power spectral density (PSD) averaged over 0°–7°N for (a) Farrar SSH, and numerically simulated (b) SSH and (c, d) velocity components at 3992-m depth from GLORYS12V1. White box is the range of frequency and wavenumber for the typical TIWs which has periods of 25–40 days and zonal wavelengths of 9°–20°.

To extend the coherence analysis shown in Figure 1c, we calculated the coherences and phases between gridded Farrar SSH and in-situ near-bottom velocity components (U_{obs}, V_{obs}), and mapped them by averaging over the frequency range of periods 25–40 days (Figures 3a–d). The coherence map between the SSH and U_{obs} (V_{obs}) exhibits high values larger than 0.6 (0.4) especially south (southwest) of the mooring observation site. These high coherences strongly suggest that both the SSH and the observed near-bottom current are related with TIW (see also Farrar, 2011; Holmes & Thomas, 2016; Farrar et al., 2021). The significant coherence also exists to the north of the mooring observation site except along the latitude around 10°N.

The positive phase relationship in the region of high coherence (> 0.6) between SSH and U_{obs} suggests that the SSH which reflects the TIWs in this region leads U_{obs}. In contrast, the negative phase relationship in the same region between SSH and V_{obs} suggests that V_{obs}

leads the SSH. These results about the phase relationship strongly indicate a southwestward phase propagation at periods 25–40 days. There is an abrupt change in phase across the latitude 10°N consistently with the cross-spectral phase estimated in the previous study where satellite-measured gridded SSH data relative to 5°N are used (Farrar, 2011). The speculation by Farrar (2011) is that this abrupt change is probably caused by a coherent superposition of TIWs with barotropic Rossby waves (BTRWs).

To verify the distribution of this BTRWs from numerically simulated barotropic velocity fields, we assume that TIW and BTRW have the same frequency and zonal wavenumber, because the TIWs will induce the BTRWs (Farrar, 2011). We would expect that the filtered barotropic velocity exhibits the BTRW induced by TIW. Further argument regarding whether the filtered barotropic velocity is BTRW induced by TIW is shown in the discussion section using the dispersion relation of BTRW.

The CEOF analysis of the filtered barotropic velocity from GLORYS12V1 clearly supports the speculation by Farrar (2011) as follows. The four maps in Figures 3e–h exhibit the first-mode CEOF phase, and the amplitude of the filtered barotropic velocity fields (U_{bt}, V_{bt}) obtained the GLORYS12V1. The phase progresses southwestward almost uniformly. The amplitude maps also show high values in the west of 115°W with slightly low values along the equator and 7°N in Figure 3g (along 4°N in Figure 3h). These tolerably uniform phase and amplitude indicate that barotropic signal with the wavelengths and periods of TIW exists over the entire study domain. The SSH data include both signal of TIW located on 0°–10°N and this barotropic signal verified from the CEOF analysis. This coexistence induces a node, which explains the non-significant coherence along approximately 10°N in Figure 3a-b.

In addition, TIWs are known to strengthen during the La Niña periods when the sea surface temperature is lower and sea surface pressure is higher than those in normal years in the equatorial eastern Pacific (Wang & Fiedler, 2006). The time series of the amplitude of the principal component of the first CEOF mode for the filtered barotropic velocity exhibits an inter-annual variation similar to that of the TIWs (Figure 3i). Large amplitudes are seen around La Niña periods (blue shades in Figure 3i). The largest amplitude occurs during the most intense La Niña periods (2007 and 2010).

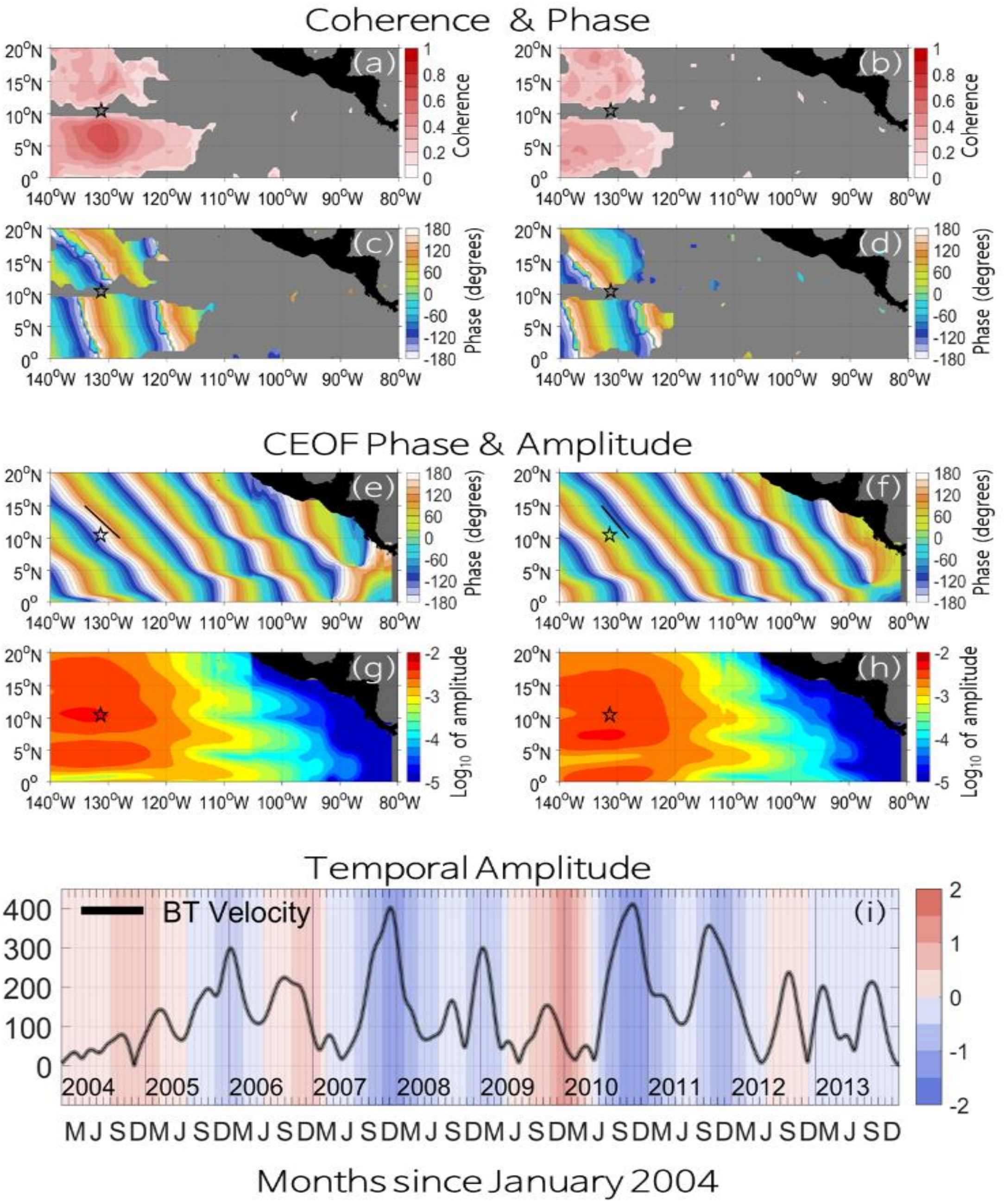

Figure 3. **(a, b)** Coherence and **(c, d)** phase maps between gridded Farrar SSH and observed near-bottom velocity components (U_{obs} and V_{obs}). **(a, b, c, d)** The left is for SSH and U_{obs}, and the right is for SSH and V_{obs}. The region with coherences under 95% significance level is gray-colored. **(e, f, g, h)** The first CEOF mode of the spatio-temporal band-pass filtered barotropic velocity components (U_{bt}, V_{bt}) obtained from the numerical simulation (GLORYS12V1) during 10 years from 2004 to 2013. The percentage of the first CEOF mode is 56.5%. The left is for U_{bt} and the right is for V_{bt}. The upper part is the phase and lower part is the amplitude. **(e, f)** Superimposed black lines are co-phase line calculated from the CEOF phase. Black stars denote the location of the mooring observation site. **(i)** The time series of the amplitude of the principal component of the first CEOF mode for the barotropic current velocity obtained from GLORYS12V1. Niño 3.4 indices (https://climatedataguide.ucar.edu/climate-data/nino-sst-indices-nino-12-3-34-4-oni-and-tni) based on a 30-year data are shown using background colors. Red denotes El Niño and blue

denotes La Niña periods, respectively.

4 Discussions

To verify our expectation that the CEOF phase of the filtered barotropic velocity is associated with TIW-induced BTRW, we compare the wavenumbers calculated from the CEOF phases to the wavenumbers obtained theoretically using the dispersion relation of the BTRW:

$$\omega = \frac{-\beta k}{k^2 + l^2} \qquad (1),$$

where ω is frequency, and k and l are the zonal and meridional wavenumbers, respectively. β is the gradient of the Coriolis parameter at specific latitudes, and we take β at 10.5°N to be 2.25×10^{-11} m^{-1} s^{-1}. Note that, in Eq. (1), the Rossby radius is assumed to be much larger than the wavelength. The comparison was performed under the assumption that the TIW and TIW-induced BTRW have the same frequency and zonal wavenumber (Farrar, 2011).

The frequencies and zonal wavenumbers of TIW were estimated to be 1.8×10^{-6} s^{-1} < ω < 2.9×10^{-6} s^{-1} (periods of 25−40 days) and -6.4×10^{-6} m^{-1} < k < -2.9×10^{-6} m^{-1} (zonal wavelengths of 9°–20° of longitude) based on the two-dimensional PSDs of Farrar SSH (see Figure 2a). The meridional wavenumbers of BTRW were calculated by substituting the frequencies and zonal wavenumbers of TIW into Eq. (1). The theoretically possible range of frequencies and wavenumbers of TIW-induced BTRW appears in the wavenumber space to be the purple region in Figure 4. On the other hand, zonal and meridional wavenumbers are also calculated using the first-mode CEOF phases as follows. The zonal wavenumbers of U_{bt} and V_{bt} by using phases at two points (10.5°N, 126.3°W and 10.5°N, 136.3°W) are estimated to be -4.18×10^{-6} m^{-1} and -4.31×10^{-6} m^{-1} and the meridional wavenumbers of U_{bt} and V_{bt} by using phases at the two points (15.5°N, 131.3°W and 5.5°N, 131.3°W) are estimated to be -5.06×10^{-6} m^{-1} and -4.03×10^{-6} m^{-1}. Note that the co-phase line is shown as the black lines in the CEOF phase maps (Figures 3e and 3f). The estimated wavenumbers based on U_{bt} and V_{bt}, are marked by blue and pink small circles in the wavenumber space (Figure 4). It is quite encouraging that they fall within the possible range of frequency and wavenumber estimated earlier, supporting the fact that the first CEOF mode is quite compatible with the TIW-induced BTRW. The direction of group velocity corresponding to the estimated possible wave frequencies and wavenumbers is northward (Figure 4). This result suggests that our in-situ near-bottom current measurements enable fluctuation due to the northward propagation of energy of TIW-induced BTRW estimated by CEOF analysis of GLORYS12V1 results.

The non-significant coherence between our in-situ near-bottom current measurements and Farrar SSH along 10°N indicates that the barotropic signals in SSH near 10°N is not correlated with the in-situ near-bottom current. This zonally non-correlated band could be observational evidence to support the speculation of Farrar (2011) that the barotropic signal in SSH is distorted by the superposition of TIWs and TIW-induced BTRWs.

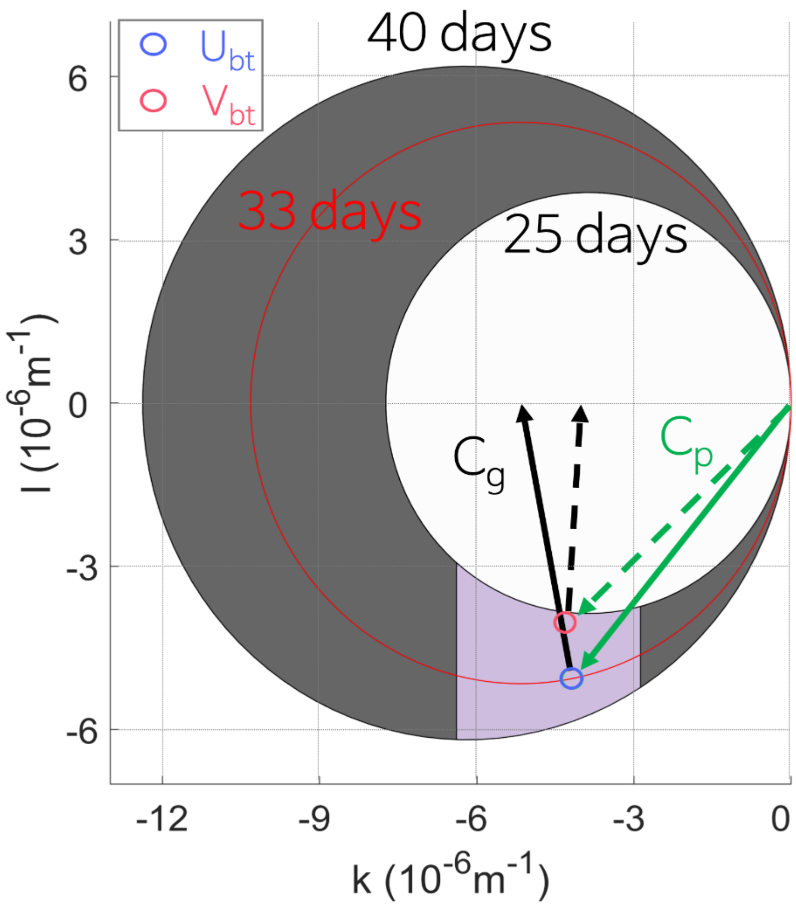

Figure 4. Dispersion relation curves of BTRW with periods of 25-40 days. The purple shading indicates theoretically possible ranges of frequency and wavenumber for TIW-induced BTRW. A large red circle corresponds to the 33-day period BTRWs. Blue and pink small circles are wavenumbers estimated from numerical results U_{bt} and V_{bt}. Green and black solid (dashed) arrows are, respectively, phase and group velocities of TIW-induced BTRW obtained from U_{bt} (V_{bt}).

5 Conclusion

Using long-term in-situ near-bottom current measurements, this study provides new evidence to confirm that the TIW-induced BTRWs propagate their energy northward above 10°N in the northeastern Pacific Ocean. The filtered time series of in-situ near-bottom current velocity shows that the TIW-induced BTRWs induce a maximum velocity of approximately 3 cm/s at the near bottom and have variations similar to those of TIWs. Our results can be the answer to the question about whether barotropic waves can actually exist in the deep ocean where the near-bottom velocities are close to zero due to bottom boundary condition (LaCasce, 2017).

It has been also evidenced from numerical simulation that this energy propagation was caused by the BTRWs, which showed inter-annual variations because the waves were derived from TIWs. The inter-annual variations of filtered velocity from numerical simulation and filtered in-situ observation suggest that the abyssal ocean responds to climate change, ENSO over the northeastern Pacific Ocean.

Our observation suggests that TIW-induced BTRWs transported the energy of the equatorial eastern Pacific Ocean to the abyssal ocean in high latitudes. The effects of TIWs transported to the abyssal ocean in a low energy environment, due to the lesser vertical gradient of density and variation of current, can lead to turbulence (Aleynik et al., 2017). The response of the bottom current is meaningful in that it is possible to affect the advection of abyssal resources, because the mooring observation site is located in the Clarion-Clippertone zone. Thus, the long-term in-situ near-bottom current velocity is also expected to improve the understanding of the distributions of mineral deposits and be used as an evaluation element in terms of abyssal mining.

Acknowledgments

Supports for this research were provided by “Test of long-term monitoring system installation for oceanic environmental changes caused by accelerated sea-ice melting in the Chukchi Sea (20210540)”, and also grant 19992001 funded by the Ministry of Oceans and Fisheries of Korea.

Open Research

The filtered near-bottom current velocity data used in figures can be downloaded https://github.com/KNLeeinha/KOMO_CM.git and will be deposited Zenodo permanently if the manuscript is accepted. A newly gridded SSH data product was provided by Farrar et al. (2021), at https://doi.org/10.5281/zenodo.4541592. GLORYS12V1 reanalysis data were provided by the CMEMS, from their web site at https://doi.org/10.48670/moi-00021.

References

Aleynik, D., Inall, M. E., Dale, A., & Vink, A. (2017). Impact of remotely generated eddies on plume dispersion at abyssal mining sites in the Pacific. *Scientific Reports*, 7(16959), 1−14. https://doi.org/10.1038/s41598-017-16912-2

An, S.-I. (2008). Interannual variation of the tropical ocean instability wave and ENSO. *Journal of Climate*, 21(15), 3680−3686. https://doi.org/10.1175/2008JCLI1701.1

Chelton, D. B., Wentz, F. J., Gentemann, C. L., de Szoeke, R. A., & Schlax, M. G. (2000). Satellite microwave SST observations of transequatorial tropical instability waves. *Geophysical Research Letters*, 27(9), 1239−1242. https://doi.org/10.1029/1999GL011047

Contreras, R. F. (2002). Long-term observations of tropical instability waves. *Journal of Physical Oceanography*, 32(9), 2715−2722. https://doi.org/10.1175/1520-0485(2002)032<2715:LTOOTI>2.0.CO;2

Farrar, J. T. (2011). Barotropic Rossby waves radiating from tropical instability waves in the Pacific Ocean. *Journal of Physical Oceanography*, 41(6), 1160−1181. https://doi.org/10.1175/2011JPO4547.1

Farrar, J. T., Durland, T., Jayne, S. R., & Price, J. F. (2021). Long-distance radiation of Rossby waves from the equatorial current system. *Journal of Physical Oceanography*, 51(6), 1947−1966. https://doi.org/10.1175/JPO-D-20-0048.1

Hernández-Guerra, A., & Nykjaer, L. (1997). Sea surface temperature variability off North-West Africa: 1981–1989. *International journal of remote sensing*, 18(12), 2539–2558. https://doi.org/10.1080/014311697217468

Holmes, R. M., & Thomas, L. N. (2016). Modulation of tropical instability wave intensity by equatorial Kelvin Waves. *Journal of Physical Oceanography*, 46(9),2623–2643. https://doi.org/10.1175/JPO-D-16-0064.1

LaCasce, J. M. (2017). The prevalence of oceanic surface modes. *Geophysical Research Letters*, 44(21), 11097–11105. https://doi.org/10.1002/2017GL075430

Lee, T., Farra, J. T., Arnault, S., Meyssignac, B., Han, W., & Durland, T. (2017). Monitoring and interpreting the tropical oceans by satellite altimetry. In D. Stammer & A. Cazenave (Eds.), *Satellite altimetry over ocean and land surfaces* (1st ed., pp. 231–270). Boca Raton, FL: CRC Press.

Legeckis, R. (1977). Long waves in the eastern equatorial pacific ocean: a view from a geostationary satellite. *Science*, 197(4309), 1179−1181. https://science.sciencemag.org/content/197/4309/1179

Legeckis, R., Pichel, W., & Nesterczuk, G. (1983). Equatorial long waves in geostationary satellite observations and in a multichannel sea surface temperature analysis. *Bulletin of the American Meteorological Society*, 64(2), 133−139. https://doi.org/10.1175/1520-0477(1983)064<0133:ELWIGS>2.0.CO;2

Lyman, J. M. (2005). Tropical instability waves as a resonance between equatorial Rossby waves. *Journal of Physical Oceanography*, 35(2), 232–254. https://doi.org/10.1175/JPO-2668.1

Lyman, J. M., Johnson, G. C., & Kessler, W. S. (2007). Distinct 17- and 33-day tropical instability waves in subsurface observations. *Journal of Physical Oceanography*, 37(4), 855−872. https://doi.org/10.1175/JPO3023.1

Moum, J. N., Lien, R. C., Perlin, A., Nash, J. D., Gregg, M. C., & Wiles, P. J. (2009). Sea surface cooling at the equator by subsurface mixing in tropical instability waves. *Nature Geoscience*, 2(11), 761–765. https://doi.org/10.1038/ngeo657

Philander, S. G. H. (1976). Instabilities of zonal equatorial currents. *Journal of Geophysical Research*, 81(21), 3725–3735. https://doi.org/10.1029/JC081i021p03725

Shinoda, T., Kiladis, G. N., & Roundy, P. E. (2009). Statistical representation of equatorial waves and tropical instability waves in the Pacific Ocean. *Atmospheric research*, 94(1), 37−44. https://doi.org/10.1016/j.atmosres.2008.06.002

Tchilibou, M., Gourdeau, L., Morrow, R., Serazin, G., Djath, B., & Lyard, F. (2018). Spectral signatures of the tropical pacific dynamics from model and altimetry: A focus on the meso-submesoscale range. *Ocean Science*, 14(5), 1283−1301. https://doi.org/10.5194/os-14-1283-2018

Thomson, R. E., & Emery, W. J. (2014). *Data analysis methods in physical oceanography*, 3rd ed., New York: Elsevier.

Wang, C., & Fiedler, P. C. (2006). ENSO variability and the eastern tropical Pacific: A review. *Progress in Oceanography*, 69(2-4), 239−266. https://doi.org/10.1016/j.pocean.2006.03.004

Warner, S. J., & Moum, J. N. (2019). Feedback of mixing to ENSO phase change. *Geophysical Research Letters*, 46(23), 13920–13927. https://doi.org/10.1029/2019GL085415

Willett, C. S., Leben, R. R., & Lavín, M. F. (2006). Eddies and tropical instability waves in the eastern tropical Pacific: A review. *Progress in Oceanography*, 69(2-4), 218−238. https://doi.org/10.1016/j.pocean.2006.03.010